Enhanced Gas Adsorption in HKUST-1@Chitosan Aerogels, Cryogels, and Xerogels: An Evaluation Study

Nisrine Hammi, Mickaele Bonneau, Abdelkrim El Kadib, Susumu Kitagawa, Thierry Loiseau, Christophe Volkringer, Sebastien Royer, Jeremy Dhainaut

Enhanced Gas Adsorption in HKUST-1@Chitosan Aerogels, Cryogels, and Xerogels: An Evaluation Study

Nisrine Hammi,[a,b*] Mickaele Bonneau,[c] Abdelkrim El Kadib,[d] Susumu Kitagawa,[c] Thierry Loiseau,[a] Christophe Volkringer,[a] Sébastien Royer,[a] Jérémy Dhainaut[a*]

[a] Univ. Lille, CNRS, Centrale Lille, Univ. Artois, UMR 8181 – UCCS – Unité de Catalyse et Chimie du Solide, F-59000 Lille, France.

[b] Univ. Lille, CNRS, INRA, Centrale Lille, Univ. Artois, FR 2638 – IMEC – Institut Michel-Eugène Chevreul, 59000 Lille, France.

[c] Institute for Integrated Cell-Material Sciences (iCeMS), Kyoto University, Kyoto 606-8501, Japan.

[d] Euromed Research Center, Engineering Division, Euro-Med University of Fes (UEMF), Route de Meknes, Rond-point de Bensouda, 30070 Fès, Morocco.

* Corresponding authors: nisrine.hammi@univ-lille.fr ; jeremy.dhainaut@univ-lille.fr

KEYWORDS: metal-organic framework; chitosan beads; drying processes; shaping; gas adsorption

ABSTRACT

This study investigates the use of chitosan hydrogel microspheres as a template for growing an extended network of the MOF-type HKUST-1. Different drying methods (supercritical CO_2, freeze-drying, and vacuum drying) were used to generate three-dimensional polysaccharide nanofibrils embedding MOF nanoclusters. The resulting HKUST-1@Chitosan beads exhibit uniform and stable loadings of HKUST-1 and were used for the adsorption of CO_2, CH_4, Xe, and Kr. The maximum adsorption capacity of CO_2 was found to be 1.98 $mmol.g^{-1}$ at 298 K and 1 bar, which is significantly higher than most MOF-based composite materials. Based on Henry's constants, thus-prepared HKUST-1@CS beads also exhibit fair selectivity for CO_2 over CH_4 and Xe over Kr, making them promising candidates for capture and separation applications.

1. INTRODUCTION

Gas purification is a significant challenge to face growing air pollution resulting from gas emissions from numerous industrial sources.[1] Different materials, such as zeolite and activated carbons,[2-3] have been extensively studied for gas capture, including primary greenhouse gases like carbon dioxide (CO_2) and methane (CH_4), or noble gases such as krypton (Kr) and xenon (Xe).[4] Metal-Organic Framework (MOF) materials, known for their large porosity, reactive metal sites, defective ligands, and framework functionalization,[5] are also widely used in gas adsorption and separation.[6] However, their applications are limited by factors such as poor thermal and chemical stability, metal site reactivity, recycling difficulties, and handling issues.[7,8]

The limitations of MOFs have impeded their industrial applications, and it is necessary to explore alternative strategies, specifically focusing on the shaping of MOFs, to overcome these challenges.[9,10] The development of MOF-based gels has greatly alleviated these problems. The gel part of MOF-based hydrogels and aerogels can support the structure of MOFs to a certain extent, which improves the stability of the MOFs and enhance their adaptability to different environments (Table S1 provides a survey of the reported MOF-based gels up to now). In this line, integrating MOFs within polysaccharide aerogels has proven to be an efficient method with significant engineering implications.[11-13] Especially, combining MOFs with pliable polymers, such as cellulose and alginate, can greatly enhance their flexibility, recyclability, and processability.[11,14] While chitosan itself offers unique benefits due to the basicity of its amino groups,[15] its nonporous structure and low specific surface area ($S_{BET} \approx 0.3\ m^2.g^{-1}$) result in low CO_2 adsorption capacity of only 0.1 $mmol.g^{-1}$) at 25 °C and 1 atm.[16] To tackle such low performance, researchers have developed chitosan aerogel composites

incorporating materials such as SBA-15, polyvinyl alcohol, polymer (PVA), clay, and graphene oxide that exhibit improved maximum CO_2 adsorption capacities ranging from 0.6 to 0.8 $mmol.g^{-1}$.[17,18] The combination of MOFs with chitosan can not only overcome these uptake limitations but also provide shaped adsorbents with enhanced adsorption capacity. For example, Fan *et al.* synthesized chitosan/ZIF-8 by annealing, resulting in a higher CO_2 capture capacity up to 0.99 $mmol.g^{-1}$ with interesting recycling abilities, owing to the carbonization of chitosan and appropriate pore regeneration during thermal treatment.[19] However, a part of the initial MOF porosity is lost during the pyrolysis process, lowering its potential performance.

While the physico-chemical properties of MOF beads towards gas sorption have been relatively well studied, few investigations have focused on the impact of the preparation pathway and the nature of drying treatment on the beads. Indeed, the gas sorption capacities of activated MOFs are significantly influenced by the synthesis route and further handling of as-synthesized samples.[20] Recent reports indicated that supercritical CO_2 treatment and freeze-drying can activate MOFs and result in significantly higher gas adsorption capacities compared to thermal or room-temperature evacuation methods.[21,22] This phenomenon is attributed to the prevention of mesopores and macropores collapse and breathing effects within the framework, resulting in increased accessibility to micropores. Our previous work involved the templating of microporous MOFs inside porous chitosan microspheres to create MOF@CS aerogel composites with hierarchical micro-, meso-, and macro-porous networks using a supercritical CO_2 drying process.[13] However, further researches are necessary to systematically investigate the impact of various parameters on the gas capture performance of MOF@CS composites, as well as to apply this strategy to better performing MOFs such as HKUST-1. HKUST-1 (Cu(II) benzene-1,3,5-tricarboxylate) is still considered to be one of

the most promising adsorbents for CO_2 capture due to its high surface area, simple and low-cost synthesis, and high density of adsorption sites. Hence, HKUST-1 powder can adsorb more than 6 $mmol.g^{-1}$ of CO_2 at 25 °C. On the other hand, this MOF structure is fragile and difficult to maintain after shaping, reducing its potential use.[8]

In this study, we developed a simple and environmentally-friendly *in-situ* synthesis route to create HKUST-1 beads with varying surface properties. We first formed a composite material by coordinating the copper salt precursor with chitosan, which was then bridged with trimesic acid as the organic linker to produce HKUST-1@CS microspheres with a hierarchical micro-/meso-porous structure and HKUST-1 loadings capacity of up to 63 wt.%. Emphasis was given to investigating the effects of the metal/NH_2 ratio as well as the activation process (CO_2 supercritical drying, freeze-drying, and vacuum drying) on the textural properties and adsorption capacity of the prepared composites. In this study the HKUST-1 crystals embedded in the HKUST-1@CS composites will offer high surface area for gas adsorption, while the chitosan will provide a robust skeleton to prevent the MOF architecture from collapsing under harsh adsorption conditions. Such material with a hierarchical porosity can be advantageously used for different gases such as CO_2, CH_4, Xe, and Kr.

2. EXPERIMENTAL SECTION

Chemicals

Chemicals used are: $Cu(NO_3)_2 \cdot 2.5H_2O$, trimesic acid, absolute ethanol, acetic acid (99%), sodium alginate (CAS number 9005-38-3) and chitosan with a high molecular weight (310000-375000 Da) and deacetylation degree of >75% (CAS number 9012-76-4). All reagents and solvents were obtained from Sigma Aldrich without further treatment.

Typical synthesis of HKUST-1@CS beads

1.5 g of high molecular weight chitosan powder were dissolved in 73 mL acetic acid aqueous solution (1 wt.%) and stirred for 24 h. A selected mass of $Cu(NO_3)_2 \cdot 2.5H_2O$ with different Cu:CS molar ratios (1:1, 2:1, 1:2) with respect to chitosan NH_2 groups (5.8 $mmol.g^{-1}$) was added to the transparent solution. Of note, a 3:1 ratio did not yield stable beads. The resulting mixture was magnetically stirred for 2 h at room temperature until complete homogenization. Dropping this solution through a 0.8 mm syringe needle into a NaOH (300 mL) bath (1 M) using a syringe induces spontaneous chitosan gelation into porous beads. After 5 h in the alkaline solution, the beads were washed with distilled water until the aqueous phase approached neutral pH, and further dehydrated by immersion for 15 min in a series of successive ethanol-water 200 mL baths (10-90, 30-70, 50-50, 70-30, 90-10, 100-0 in volume).[23] The beads were next placed in an alcoholic solution (20 mL) containing trimesic acid (H_3BTC) with a Cu:H_3BTC molar ratio of 1:2 at 80 °C for 48 h. The diffusion of the H_3BTC ligand within the beads and its further condensation with the previously entrapped copper cations promotes the growth of the HKUST-1 crystals within the resulting composite. Indeed, typical octahedrally-shaped crystals of HKUST-1 are clearly observed in the beads (Fig. 1). For now, such strategy represented in Scheme 1 can only be applied with MOFs whose metal clusters or ions are stable under strongly basic pH, and whose linker can be dissolved in conditions where the stability of the chitosan beads is maintained.

The solvent was then removed from the wetted HKUST-1@CS scaffolds following three different drying techniques, namely:

a- Supercritical CO_2 drying, which was carried at 73 bar and 35 °C. The given aerogels are named HKUST-1@$CS_{1:1}$A.

b- Vacuum drying, which was done in a standard vacuum oven at room temperature for 24 h. The obtained xerogels are named HKUST-1@$CS_{1:1}$X.

c- Freeze drying, involving the rapid freezing of alcogel beads using liquid nitrogen. These frozen beads are then placed in a freeze-dryer. The resulting cryogels are known as HKUST-1@CSx:yC, where "x:y" represents the Cu:CS molar ratio employed.

For comparison, pure chitosan beads, denoted as CS, were also prepared similarly and dried under freeze-drying conditions. Besides, in order to unveil any possible role of nitrogen, nitrogen-free beads were prepared by following the same procedure except that chitosan was replaced by sodium alginate (SA). The obtained sample was denoted **HKUST-1@SA$_{2:1}$C.** The HKUST-1 material was synthesized according to the procedure outlined in the literature, resulting in a high-quality and pristine product.[24]

Procedures for HKUST-1@CS gas adsorption

Before measurement, about 50 mg of the sample was degassed for 8 h at 100 °C under a primary vacuum. CO_2 (99.995, Air Liquide), Xe (99.997, Linde Gas), and Kr (99.9999 Linde Gas) single-component gas sorption isotherms were collected with a Micromeritics ASAP 2020 automated gas sorption system. The desired sorption temperature (273, 298, or 323 K) was controlled with a thermostatic glycol bath (Huber, Pilot one). High-pressure CH_4 (>99, Air Liquide) sorption isotherms were measured with a BEL Japan BELSORP-max volumetric adsorption instrument at 298 K and up to 70 bar.

Materials characterization

Nitrogen (N_2) physisorption isotherms were recorded at 77 K on a Micromeritics Tristar II automated gas sorption system. Before analysis, the samples were outgassed under a dynamic vacuum at 120 °C overnight. The specific surface area was determined using the multipoint B.E.T. algorithm in the p/p_0 range from 0.10 to 0.25 and the total pore volume is determined on the adsorption branch at $p/p_0 = 0.98$. The pore diameters and the pore size distributions were calculated

from the desorption branch using the Barrett–Joyner–Halenda (BJH) and non-local density functional theory (NLDFT) methods.

A Micromeritics Autopore IV 9500 penetrometer was used to probe the mesopores and macropores by mercury intrusion. A contact angle of 130° was assumed in the pore size calculations.

X-ray diffraction (XRD) was performed using a Bruker X-ray AXS D8 Advance diffractometer in Bragg-Brentano configuration and equipped with a LynxEye Super Speed detector. XRD patterns were recorded with Cu Kα radiation (λ = 0.154 nm, 40 kV, 30 mA) in the 10–80° 2θ range with a 0.02° 2θ step. Phase identification was made by comparison with the ICDD database.

Fourier transform infrared spectroscopy (FTIR) spectra were monitored using a NICOLET iS10 spectrometer.

A KRATOS Axis Ultra spectrometer operated under ultrahigh vacuum conditions, using a twin Al X-ray source (1486.6 eV) at pass energy of 40 eV, was used for the X-ray photoelectron spectroscopy (XPS) analyses. The solid, in the form of a pellet, was fixed on a copper holder with copper tape. The binding energy values were estimated, positioning the C 1s peak of contaminant carbon at a B.E. of 285.0 eV. The Casa XPS software package was used for data analysis.

Thermogravimetric curve profiles were obtained on TA instruments SDT2960 under the constant flow of simulated air (20 vol% O_2-80 vol% N_2) in the range of 25-900 °C with a 5 °C/min heating rate.

Scanning electronic microscopy (SEM) images were obtained using a JEOL JSM-7800F LV After the sample covering with 10 Å of the carbon layer.

A Vinci Technologies Versatile Crushing Strength Tester was used to perform crushing tests on single solids, using a set of flat anvil and a hammer. The load applied was recorded by the force sensor as a function of the displacement of the punch at a constant speed of 0.6 mm/min until failure,

happening at the ultimate crushing strength of the solid. For each sample, 10 representative solids were crushed and the resulting values, given in Newton, were averaged.

3. RESULTS AND DISCUSSION

The synthesis of HKUST-1@CS beads was achieved through an *in-situ* method as illustrated in Scheme 1. The initial formation of the copper-chitosan complex is facilitated by the favored coordination between the Cu^{2+} cations and the amino groups of chitosan.[12] Further dropwise addition of this complex into a NaOH bath results in the generation of $Cu(OH)_2$-chitosan alcogels due to the insolubility of chitosan in alkali solutions.

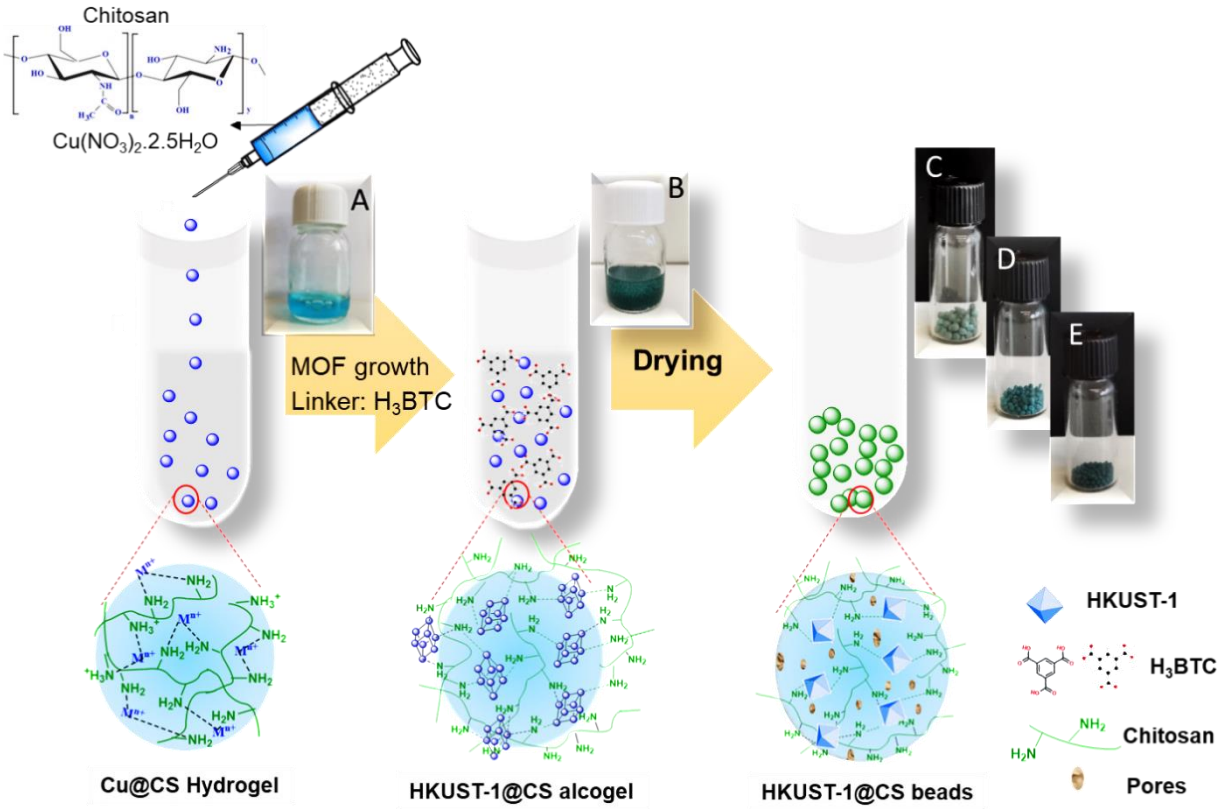

Scheme 1. Illustration of the multistep preparation procedure for HKUST-1@CS beads. The interplay between the biopolymer, the metal precursor and the ligand is presented along these steps. The digital photos show: A) Cu^{2+}-Chitosan solution; B) HKUST-1@CS alcogel; C) HKUST-1@CS aerogel; D) HKUST-1@CS cryogel, E) HKUST-1@CS xerogel.

The as-prepared HKUST-1@CS alcogel composites were dried by different techniques (supercritical CO_2, freeze-drying, and vacuum drying). The use of carbon dioxide is privileged for the supercritical treatment as it reaches its supercritical state at a relatively low temperature of 31 °C, compared to 373 °C required for water and 513 °C for ethanol, making it suitable to dry soft, labile materials without decomposition, as it would be the case of polysaccharides. As a result, the HKUST-1@CS alcogel microspheres can be converted into highly porous aerogels without any noticeable damage or structural collapse. This successful preservation of the microsphere dimensions during the transition from alcogels to aerogels confirms the absence of any severe collapsing or densification of the chitosan matrix. Scheme 1 and Figure S1 provide clear visual evidence of the preserved shape of the microspheres in the dry samples. However, it is important to highlight that the xerogels, with an average size of 1.1 mm, demonstrate considerably greater shrinkage compared to both the cryogels and aerogels, which have both an average size of 1.5 mm, while the initial size of the hydrogels before drying was 1.8 mm.

The chemical structures of the different HKUST-1@CS composites were analyzed using FT-IR (Fig. S2). All HKUST-1@CS beads exhibit the typical absorption peaks of chitosan, including the carbonyl band (C=O-NHMe) at 1646 cm^{-1} and the amine band (NH_2) at 1589 cm^{-1}.[13,25] In comparison to pure chitosan beads, new absorption bands corresponding to metal-organic coordination (Cu-O-C) and metal-chitosan chelation ($H_2N\rightarrow Cu$ and $HO\rightarrow Cu$) are observed. Specifically, the absorption band at 727 cm^{-1} is attributed to Cu-O stretching,[12] resulting from either metal-organic coordination in MOFs or chelating bonds between the metal and hydroxyl groups of chitosan. Additionally, a new band at 1371 cm^{-1}, derived from C=C stretching in the aromatic ring of the linker, is observed.[26] Furthermore,

the NH_2 band is shifted towards lower wavenumbers in the spectrum of HKUST-1@CS beads (1554 cm^{-1} for **HKUST-1@CS$_{1:2}$C**, 1560 cm^{-1} for **HKUST-1@CS$_{1:1}$C**, and 1550 cm^{-1} for **HKUST-1@CS$_{2:1}$C**), indicating electron density donation from NH_2 to the copper center (NH_2→Cu). Finally, the visible bands at 454-477 cm^{-1} are characteristic of the Cu-N stretching band.[12,21]

Powder XRD measurements (Fig. S3a-b) revealed typical diffraction Bragg peaks related to the crystalline HKUST-1 phase in **HKUST-1@CS$_{1:1}$C** and **HKUST-1@CS$_{2:1}$C** samples, even if slightly broader lines are observed compared to those of the pristine HKUST-1 (at 11.6° 2θ - (222) plane, FHWM of HKUST-1, **HKUST-1@CS$_{2:1}$C** and **HKUST-1@CS$_{1:1}$C** is 0.156°, 0.158° and 0.168°, respectively) (Fig. S3c). As expected, the Cu:CS ratio thus has an impact on the final size of the crystals, with larger Cu loadings facilitating the crystals growth. The powder XRD diagram of **HKUST-1@CS$_{1:2}$C** composite exhibited a partially amorphous phase, indicated by the broad bump in the 15-40° (2θ) range (Fig.S3a), together with less intense Bragg peaks attributed to the HKUST-1 phase. This may arise from the strong bonding of copper ions by amine groups emanating from chitosan biopolymer in excess, impeding their further coordination with H_3BTC ligands. To evaluate the role of NH_2 from chitosan, it is worth noting that alginate was utilized as a reference giving the material **HKUST-1@SA$_{1:1}$C**. An almost fully amorphous XRD pattern was observed, with a single weak reflection at around 11.6° (2θ), indicating the occurrence of a very small amount of HKUST-1. This may be attributed to the competitive binding of alginate with the copper ions or organic H_3BTC ligands during the self-assembly process of HKUST-1. Additionally, it is possible that the formation of complexes during the self-assembly process could interfere with the formation of HKUST-1, leading to the observed amorphous pattern,

representative of the polymeric polysaccharide structuration. When comparing the same sample dried *via* different methods, it could be observed that XRD patterns of **HKUST-1@CS$_{1:1}$C**, **HKUST-1@CS$_{1:1}$A**, and **HKUST-1@CS$_{1:1}$X** composites displayed similar Bragg reflections, as shown in Figure S3b, indicating that the crystalline HKUST-1 structure was preserved despite the drying method used. This result is consistent with the literature.[27] The SEM analyses of the HKUST-1-chitosan composite series provide valuable insights into the internal structure of the chitosan microspheres (Fig. 1, S4a). On the external surface of the aerogel beads, truncated particles with an octahedral shape were observed (Fig. 1a-c), while smaller HKUST-1 particles grown inside the polysaccharide network became visible upon halving the beads (Fig. 1d,e, S4a). Notably, there was a significant difference in particles size between those formed on the surface and those grown internally. For instance, **HKUST-1@CS$_{1:1}$A** exhibited an average particle size of 14 µm on the surface (Fig. 1b,c, S4b) compared to approximately 2 µm in the bulk (Fig. S4a). This disparity can be attributed to two factors: (i) the confinement effect within the microspheres, where the nitrogen-containing functional groups could impede the growth of HKUST-1 particles, leading to their smaller size; (ii) the formation of larger HKUST-1 particles due to the presence of metal ions near the outer surface, which offers more freedom and space for network expansion and crystal growth. Furthermore, irregular spherical pores with an estimated size of 2.55 µm were observed in **HKUST-1@CS$_{1:1}$A** (Fig. S4). This observation further supports the feasibility of creating porous aerogels, which can be achieved through hydrogel swelling or by modifying the hydrogen bonding between adjacent biopolymer fibrillar chains. These alterations likely occur during the solvent exchange or removal process, which is a crucial step in drying polysaccharides.[13] Additionally, in **HKUST-1@CS$_{1:1}$C**, a

macroscopic porosity was observed (Fig. 1d, S4), which can be attributed to the formation of ice crystals. These ice crystals create skeletal walls with large pores at the upper level.[28] As expected, the particles size attributed to the presence of crystalline HKUST-1 increased with the ratio HKUST-1:CS (Fig. 1e-f and S4), while increasing the amount of chitosan enhanced the coating of the particles as taking place within **HKUST-1@CS$_{1:2}$C**. This indicates that the polysaccharide acts as both a structure-directing agent and a growth inhibitor during the MOF crystallization. Mapping the location of carbon and nitrogen versus the copper reveals the uniform distribution of these elements within the microspheres and thus the homogeneous dispersion of HKUST-1 particles (Fig. 1g,h and S4).

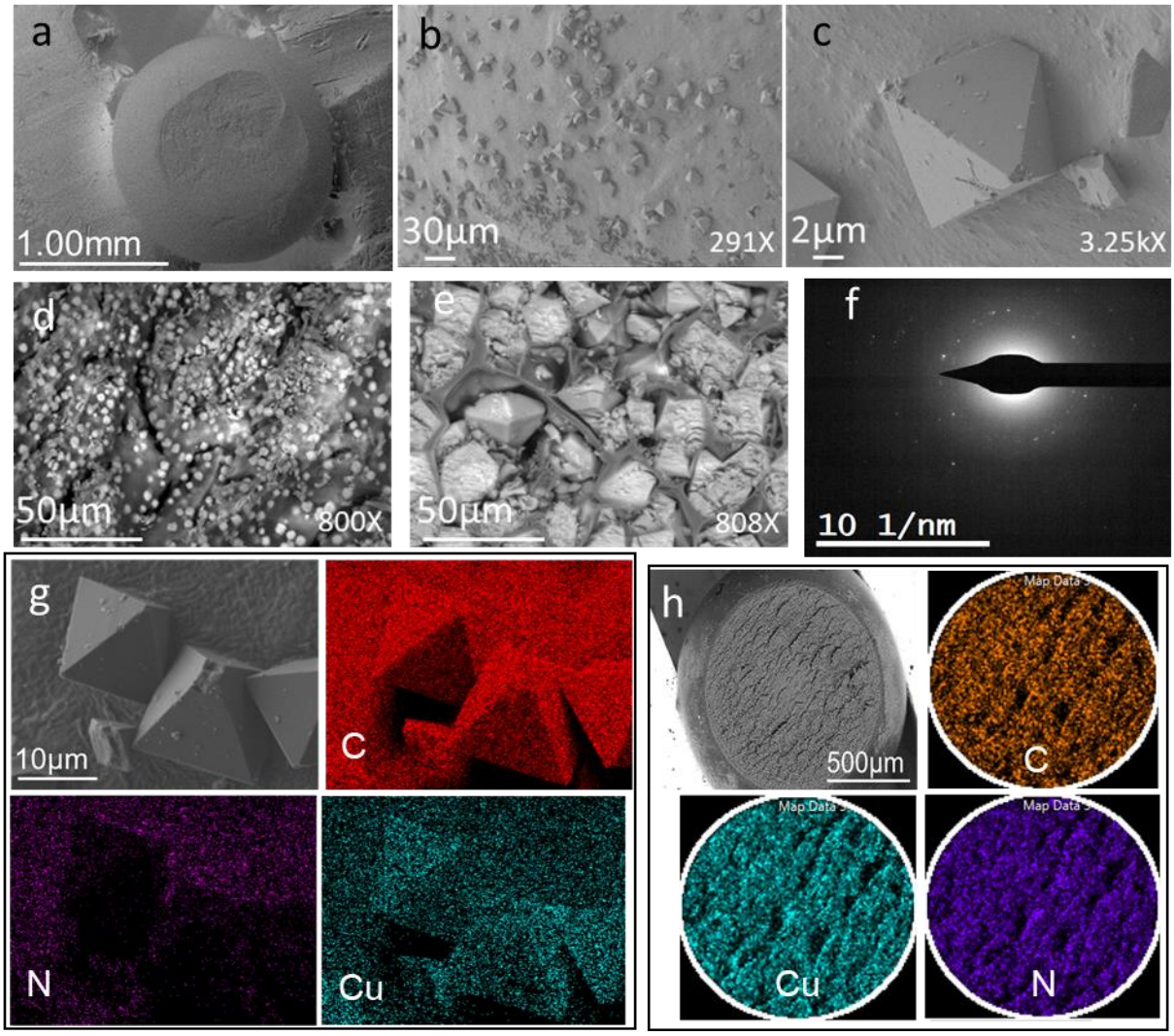

Fig. 1. SEM images of **HKUST-1@CS$_{1:1}$A, HKUST-1@CS$_{2:1}$C** and **HKUST-1@CS$_{2:1}$C**. (a-c,f) SEM image and selected area electron diffraction (SAED) pattern of **HKUST-1@CS$_{1:1}$A**, (d) cross-section view of **HKUST-1@CS$_{1:1}$C**; (e) cross-section view of **HKUST-1@CS$_{2:1}$C**; (g,h) EDS elemental mappings of **HKUST-1@CS$_{1:1}$A.**

The thermal stability of these nanocomposites, as well as their MOF loadings, were further assessed using thermogravimetric analysis under airflow (Fig. S5). HKUST-1 MOF powder shows two distinct weight losses. The first weight loss at 150 °C is attributed to the removal of solvent and metal-coordinated water. Subsequently, a narrow temperature range starting at ≥ 300 °C shows a second weight loss, which corresponds to the decomposition of the trimesate linker. Chitosan (CS) also shows two weight loss steps: one from 150 to 350 °C, corresponding to the dehydration of glycosidic rings as well as initial thermal depolymerization, and a second one exothermic from 350 to 550 °C and attributed to the decomposition of deacetylated and acetylated units. The composite beads, being a mixture of both materials, present all of these features. While native chitosan microspheres are completely burnt off from a temperature of 580 °C, the resulting hybrid materials display a mineral residue varying from 11 wt.% to 25 wt.% up to 800 °C. This residual solid can be attributed to the conversion of HKUST-1 into copper oxide (CuO). Based on this residue, the HKUST-1 loadings for **HKUST-1@CS$_{1:2}$C**, **HKUST-1@CS$_{1:1}$C**, **HKUST-1@CS$_{2:1}$C** and **HKUST-1@SA$_{1:1}$C** are recalculated as 40 wt.%, 58 wt.%, 63 wt.% and 28 wt.%, respectively (Table S2). Excepted for **HKUST-1@SA$_{1:1}$C**, these values closely approximate the theoretical values. Under ideal conditions, it can be assumed that the copper precursor is fully incorporated, indicating that the added copper and linker are used for the formation of HKUST-1 (Table S2).

The textural properties of the different HKUST-1@CS composites were first characterized using N_2 adsorption-desorption measurements shown in Figure S6 and summarized in Table 1. For **HKUST-1@CS$_{2:1}$C** and **HKUST-1@CS$_{1:1}$C** composites, Type IV isotherms with a sharp increase in the micropore and the large mesopore regions and type H2 hysteresis loops are observed, which suggests that these beads present a hierarchical pores network. This shape is very typical of chitosan cryogels presenting moderate surface area, 71 $m^2.g^{-1}$ in our case (Table 1),[29] and for which the entanglement of the fibrils leads to forming large mesopores connected to macropores. The specific surface areas of **HKUST-1@CS$_{2:1}$C**, **HKUST-1@CS$_{1:1}$C** and **HKUST-1@CS$_{1:2}$C** are 502, 527 and 249 $m^2.g^{-1}$, respectively. Significantly increasing the amount of chitosan in **HKUST-1@CS$_{1:2}$C** decreases the specific surface area. This phenomenon is mostly ascribed to the dilution of the HKUST-1 within the less porous biopolymer as well as partial pore blockage by the polymer chains. Of note, **HKUST-1@CS$_{1:1}$C** presents intercrystalline mesopores in the 2 to 50 nm region (Fig. S7), which are the result of smaller crystals size and their interactions with the chitosan matrix. Their presence affects the calculation of the specific surface area, resulting in a value that is higher than for **HKUST-1@CS$_{2:1}$C** with a lower MOF loading. However, the microporous surface and volume as determined by the BJH method are in accordance with the MOF loading. Finally, nitrogen sorption of **HKUST-1@SA$_{1:1}$C** reveals that the material is dense and devoid from any appreciable open framework since no N_2 sorption could be performed. As stated above, this material is mostly amorphous with copper mostly interacting with alginate and H_3BTC species entrapped within the polymer.

The effect of the drying method on the porous structure was further investigated. The surface area of the **HKUST-1@CS$_{1:1}$X** xerogel (460 $m^2.g^{-1}$) was lower than the **HKUST-1@CS$_{1:1}$A**

aerogel (531 $m^2.g^{-1}$) and **HKUST-1@CS$_{1:1}$C** cryogel (527 $m^2.g^{-1}$), which suggests the limited ability to maintain the porosity *via* vacuum drying. In addition, **HKUST-1@CS$_{1:1}$X** xerogel exhibited a narrower BJH pore size distribution (7.4 nm) (Fig. S7, Table 1) than the aerogel and cryogel counterparts (> 14 nm). These results are consistent with the absence of capillary forces and surface tension effect during supercritical CO_2 and freeze-drying.[30] The micropore size distribution (Fig. S7) further shows the presence of 1.2 and 1.7 nm diameter pores in all samples, consistent with the contribution of HKUST-1 microporosity. This size distribution remains constant with varying metal/NH_2 ratio, pledging for neglectable MOF pores filling by the biopolymer. Notably, **HKUST-1@CS$_{1:1}$A** shows a remarkably higher total pore volume (1.71 $cm^3.g^{-1}$) than those of **HKUST-1@CS$_{1:1}$C** (0.8 $cm^3.g^{-1}$) and **HKUST-1@CS$_{1:1}$X** (0.63 $cm^3.g^{-1}$), which is ascribed to complete pore evacuation via supercritical CO_2 drying. Crucially, both the size and volume of the mesopores obtained in this study vary with drying conditions.

To further investigate the presence of meso- and macroporosity within the beads, mercury intrusion measurements were performed (Fig. S8). The pore size distributions of **HKUST-1@CS$_{1:1}$A** and **HKUST-1@CS$_{1:1}$C** exhibit a bimodal feature: except for a main peak centred at 13 nm and 8 nm, respectively, indicating the prevalence of mesopores, a relatively weak and broad distribution with peaks centred at 0.240 µm and 5 µm, respectively, can also be observed, indicating the existence of a various range of macropores. In contrast, for **HKUST-1@CS$_{1:1}$X**, only macropores in the range of 4-6 µm are retained, in line with the densification of the beads after activation. Thus HKUST-1@CS features a multimodal porous structure consisting of interconnected pores ranging from micro-, meso- to macropores. Such hierarchical porosity may be beneficial to adsorb or separate gas.

Table 1. Textural properties for the HKUST-1@CS beads and the pristine HKUST-1

Samples	S_{BET} [a] (m^2g^{-1})	S_μ [b] (m^2g^{-1})	V_{tot}[c] (cm^3g^{-1})	V_μ[d] (cm^3g^{-1})	V_{mes}[e] (cm^3g^{-1})	D_μ [f] (nm)	D_{mes} [g] (nm)
CS	71	NA	0.13	NA	NA	NA	9.6
HKUST-1	1337	1145	0.77	0.60	0.17	1.2	-
HKUST-1@$CS_{1:1}$C	527	323	0.8	0.13	0.67	1.2(1.7)	14.2
HKUST-1@$CS_{1:1}$A	531	337	1.71	0.16	1.55	1.2(1.7)	14.2
HKUST-1@$CS_{1:1}$X	460	290	0.63	0.11	0.52	1.2(1.7)	7.4
HKUST-1@$CS_{1:2}$C	249	137	0.23	0.05	0.18	1.2(1.5)	4/19
HKUST-1@$CS_{2:1}$C	502	420	0.32	0.16	0.16	1.2(1.5,1.7)	4.1/43
HKUST-1@$SA_{2:1}$C	NA	NA	NA	NA	NA	NA	NA

[a] BET surface area; [b] micropore surface area; [c] total pore volume obtained at P/Po = 0.98; [d] micropore volume with t-plot method; [e] Mesopore volume is determined by subtracting the micropore volume from the total volume; [f] NLDFT pore diameters, with secondary pore distributions noted in brackets; [g] BJH pore diameter calculated on desorption branch; NA: not applicable.

One of the major issues of highly porous solids is their mechanical stability. Here, the mechanical stability of **HKUST-1@$CS_{1:1}$A** towards compression was evaluated through crushing tests (Fig. S9). An average crush strength of 12.35 N was measured over 10 beads. For comparison, commercial catalysts for refining processes present a crush strength of 20 N or higher, demonstrating that such produced HKUST-1@CS beads are well-suited for practical applications.[8]

Insight into the chemical composition was gained by comparative XPS analysis of HKUST-1 and **HKUST-1@$CS_{1:1}$A** (Fig. S10). N 1s spectra were decomposed into two peaks with binding energies at 397.6 ± 0.2 eV and 399.0 ± 0.2 eV, which can be attributed to free NH_2 groups and the coordinated NH → Cu, respectively. This further corroborates the intimate interaction of Cu species with nitrogen.[31] A close look at the XPS spectra of Cu 2p3/2 for the two materials HKUST-1 and **HKUST-1@$CS_{1:1}$A** reveals intense broad lines at 934.5 eV for **HKUST-1@$CS_{1:1}$A** accompanied by satellites centred at 939–945 eV corresponding to the Cu^{2+} state.[31,32] The similarities between the XPS profiles of HKUST-1 and **HKUST-1@$CS_{1:1}$A** indicate that most of the copper entrapped in the chitosan microspheres are

coordinated into HKUST-1 phase, which excludes the predominance of nanosized copper clusters or molecular copper that could be linked to chitosan.[33]

CO_2 uptake by HKUST-1@CS beads

The adsorption capacity of HKUST-1@CS materials typically depends on the physico-chemical nature of the sorbents, and in this specific case, on the potential synergistic effects arising from CS-MOF interactions. Especially, the surface area and micropore volume, and the presence of basic N atoms can significantly affect the adsorption performance. In this context, the effect of the drying method over the CO_2 uptake of HKUST-1@CS beads has first been investigated. Figure 2a shows the CO_2 adsorption capacity of the three samples (**HKUST-1@$CS_{1:1}$A**, **HKUST-1@$CS_{1:1}$C,** and **HKUST-1@$CS_{1:1}$X**) at 273 K up to 1 bar. In line with the measured specific surface areas, the CO_2 uptakes of all HKUST-1@CS adsorbents are significantly higher than that of the neat chitosan (0.083 mmol.g^{-1}) (Fig. S11), with maximum capacities of **HKUST-1@$CS_{1:1}$C**, **HKUST-1@$CS_{1:1}$A,** and **HKUST-1@$CS_{1:1}$X** reaching 2.68 mmol.g^{-1}, 2.54 mmol.g^{-1} and 2.28 mmol.g^{-1}, respectively. Thus, for the same material, the CO_2 capacity at equilibrium is mainly governed by the available micropore volume.[34] Especially, the CO_2 uptake of the HKUST-1@$CS_{1:1}$C composite, with a HKUST-1 loading of only 58 wt.%, reached 2.68 mmol.g^{-1}. In contrast, HKUST-1@$CS_{1:1}$A achieved a CO_2 uptake of 2.54 mmol.g^{-1}. It is hypothesized that this difference in CO_2 adsorption between HKUST-1@$CS_{1:1}$A and HKUST-1@$CS_{1:1}$C may be attributed to the quicker diffusion for CO_2 molecules within the cryogel structure due to the presence of radial macropores. Remarkably, HKUST-1@$CS_{1:1}$C's CO_2 uptake value corresponds to 42 % of the CO_2 adsorption capacity exhibited by pure HKUST-1, which has a capacity of 6.44 mmol.g^{-1} (Fig. S12). It is worth noting that the reported literature value for pure

HKUST-1 is typically up to 6.85 mmol.g^{-1}.[35] Thus, it can be concluded that the adsorption capacity attributed to the inclusion of HKUST-1 in the composite was effectively preserved, despite a slight reduction caused by variations in pore accessibility and differences in pore size distribution among the composites.

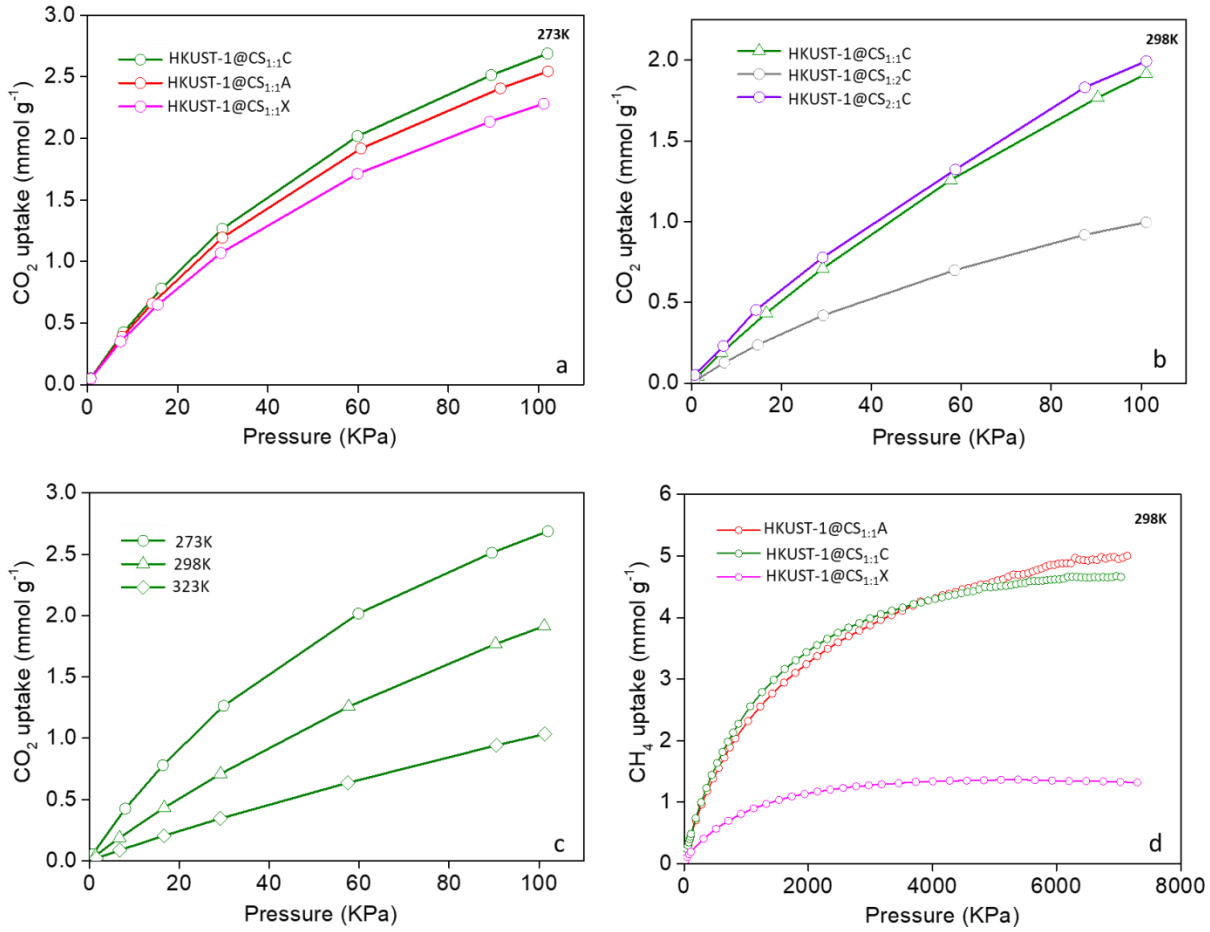

Fig. 2. (a) Effect of the drying method on CO_2 uptake of HKUST-1@CS beads; (b) Effect of HKUST-1 loading on CO_2 uptake at 298 K using cryogels; (c) Effect of the sorption temperature on CO_2 uptake CO_2 adsorption using **HKUST-1@CS$_{1:1}$C**; (d) Influence of the operating pressure on CH_4 uptake by HKUST-1@CS beads at ambient temperature.

Figure 2b shows a comparison of the adsorption behaviour using cryogels with different HKUST-1 loadings at 298 K up to 1 bar. The adsorption capacity for the sorbent **HKUST-1@CS$_{2:1}$C** containing 63 wt.% of HKUST-1 is 1.98 mmol.g^{-1} while the capacities of

HKUST-1@CS$_{1:1}$C and **HKUST-1@CS$_{1:2}$C** beads are 1.91 mmol.g^{-1} and 0.99 mmol.g^{-1}, respectively. These results are in accordance with the lower HKUST-1 loading in the composite materials, and the related decrease in specific surface area and total pore volume. The effect of temperature on CO_2 uptake using **HKUST-1@CS$_{1:1}$C** hybrid sorbent at 273, 298, and 323 K was also investigated (Fig. 2c). In line with the facilitated desorption of CO_2 molecules at higher temperatures,[36] the CO_2 maximum capacity decreases with increasing the temperature: from 2.68 mmol.g^{-1} at 273 K to 1.03 mmol.g^{-1} at 323 K.

To the best of our knowledge, the CO_2 uptake reported for **HKUST-1@CS$_{1:1}$C** composite presented in this work at 298 K is twice as high as previously reported chitosan-based shaped sorbents (Table 2), and competes with liquid amines while being easily reusable.[37] For instance, Hsan and coworkers reported a CO_2 uptake around 0.257 mmol.g^{-1} at 1 bar and 298 K, for a CS grafted graphene oxide aerogels.[38] In another study, Fan *et al.* synthesised chitosan/ZIF-8 by an annealing process to enhance CO_2 capture to 0.99 mmol.g^{-1}, which was higher than that of as-synthesized ZIF-8/CS spheres (0.679 mmol.g^{-1}).[19] We also recently reported the preparation of ZIF-67/CS microspheres, with CO_2 uptakes at 298 K up to 0.76 mmol.g^{-1}.[39]

Table 2: Comparison of the CO_2 adsorption of related porous aerogels.

Sorbent	Conditions	Types of material	Shape	S_{BET} (m^2g^{-1})	CO_2 uptake mmol.g^{-1}	Ref
CSGO	25°C, 1 bar	CS grafted graphene oxide	Aerogels	33	0.26	38
ZIF-67/CS$_{2:1}$	25°C, 1bar	Chitosan/ZIF-8	Beads	1197	0.76	39
CTS-GO-5%	25°C, 1bar	Chitosan and grapheme oxide	Aerogels	<40	0.60	40
PIL-chitosan	25°C, 1 bar	Poly(ionic liquid)s	Aerogels	449	0.70	41
CS-(4-formyltriphenylamine)	25°C, 5bar	Chitosan with 4-formyltriphenylamine	Gel	52.78	0.85	42
CS/ZIF-8	25°C	Chitosan/ MOF	Beads	626	0.99	19
GZA8	25°C, 1bar	Graphene/ZIF-8	Aerogel	1099	0.99	43

HKUST-1@$CS_{2:1}$C	25°C, 1bar	HKUST-1/chitosan	Beads	502	1.98	This work

For practical applications, not only should the CO_2 uptake at 298 K be around 2 mmol.g^{-1} or higher, but the isosteric heats of adsorption (Qst) should also be below 50 kJ.mol^{-1} for facile sorbent regeneration.[37] Several reported data obtained for amine-modified porous substrates showed that their values of adsorption heat range from 20–50 kJ/mol, which indicates weak chemisorption.[18,44] Primo *et al.*[45] reported that the Qst values of CO_2 adsorption using CS-derived spherical carbons were in the range of 19-35 kJ mol^{-1}. Very recently, we found that the values of Qst for CO_2 adsorption using ZIF-67/$CS_{2:1}$ beads were in the range of 11.6–44.1 kJ mol^{-1}.[39] Herein, the Qst values of **HKUST-1@$CS_{1:1}$C** were calculated from the CO_2 sorption isotherms measured at different temperatures (Fig. 2c) using the Clausius–Clapeyron equation as plotted in Figures S13-S14.[46] The maximum value of Qst (~22.6 kJ mol^{-1}) indicates that weak interactions are involved, making **HKUST-1@$CS_{1:1}$C** a promising candidate for CO_2 capture storage and reutilization (CCUS).

High-pressure CH_4 uptake and CO_2/CH_4 selectivity

HKUST-1 has been extensively investigated for methane storage and release in automotive applications, as it outperforms commercial activated carbons. In this case, both gravimetric and volumetric uptakes should be considered. The total CH_4 adsorption capacities of the different studied samples at 298 K are plotted for various pressures in Figure 2d. At low pressures, **HKUST-1@$CS_{1:1}$C** shows the highest CH_4 uptakes supported by the MOF microporosity, followed by nearly identical CH_4 uptakes for the **HKUST-1@$CS_{1:1}$A** beads. However, in the high-pressure regime where pore volume effects are important and the energy and affinity-driven adsorption sites are occupied, the meso/macroporous nature of the HKUST-1@CS beads becomes evident. This distinctive structure facilitates enhanced

accessibility to additional adsorption sites, leading to a substantial adsorption capacity of 4.70 mmol.g^{-1} at 50 bar. The much lower CH_4 adsorption capacity with **HKUST-1@CS$_{1:1}$X** beads and saturation from 40 bar are unexpected and might be related to their densification during drying. These findings highlight the importance of considering both microporous and meso/macroporous structures when designing high-performance adsorbents for gas storage and separation applications.

It is worth noting that the adsorption capacity of these composite beads is comparable to that of the previously reported HKUST-1 3D-printed solids, which exhibited an adsorption capacity of 5.18 mmol.g^{-1} at 298 K and 50 bar.[47] However, it should be emphasized that the 3D-printed solids had a significantly higher surface area (S_{BET} = 1200 m^2.g^{-1}).[47] However, the reported adsorption capacity of pure HKUST-1 powder at 298 K and 35 bar, which is 10.13 mmol.g^{-1} surpasses that of the composite beads.[48]

One way to valorize CO_2 is through its use as a reagent. Notably, methanation allows to transform CO_2 into CH_4 ($CO_2 + 4H_2 \rightarrow CH_4 + 2H_2O$) for energy applications.[49] Thus, it is of practical importance to develop selective sorbents to purify the gas flow downstream of the reaction. To evaluate the CO_2 separation performance of **HKUST-1@CS$_{1:1}$C**, single component CO_2, and CH_4 isotherms were collected at 1 bar at 298 K. The adsorption capacity of **HKUST-1@CS$_{1:1}$C** at 298 K for CH_4 is 0.48 mmol.g^{-1}, in comparison with 1.91 mmol.g^{-1} for CO_2 (Table S3). Figure S15a shows that the CO_2 and CH_4 adsorption isotherms have initial slopes of 1.93 and 0.44, respectively. By calculating the ratio of Henry's constants, the **HKUST-1@CS$_{1:1}$C** beads present a predicted CO_2/CH_4 selectivity of 4.4 at 298 K, indicating preferential adsorption of CO_2. This selectivity further improves to 6.8 at 273 K and 1 bar (Fig. S15b), suggesting that the material is more selective towards CO_2 at lower temperature and pressure conditions.

Furthermore, the adsorption capacity of **HKUST-1@CS$_{1:1}$X** at 298 K for CH_4 is 0.19 mmol.g^{-1}, in comparison with 1.33 mmol.g^{-1} for CO_2. Figure S15c shows that the CO_2 and CH_4 adsorption isotherms have initial slopes of 1.33 and 0.16, respectively. By calculating the ratio of Henry's constants, the **HKUST-1@CS$_{1:1}$X** beads present a predicted CO_2/CH_4 selectivity of 8 at 298 K, indicating even more preferential adsorption of CO_2.

Moreover, it has been reported that HKUST-1 may be functionalized to further improve this selective adsorption, for example by incorporating calcium ions in the framework, which is beyond the scope of this study.[50] Overall, these findings indicate that **HKUST-1@CS$_{1:1}$C** may be used for CO_2 separation owing to the stronger attraction of CO_2 by the polar functional groups of **HKUST-1@CS$_{1:1}$**C.

Xe/Kr capture by HKUST-1@CS beads

As a way to showcase the material's versatility for gas separation, we also performed adsorption tests with xenon and krypton noble gases. This application is of growing interest for the valorisation of gaseous fission products.[9] The experiments conducted at 273 K and 1 bar using **HKUST-1@CS$_{1:1}$C** revealed an adsorption capacity of 1.61 mmol.g^{-1} for Xe, compared to only 0.29 mmol.g^{-1} for Kr (Fig. S16). This leads to a predicted Xe/Kr selectivity of 6.2 based on Henry's constants (Fig. S17), which is slightly lower than that of the pristine HKUST-1 (8.1). The reduction in selectivity observed in the composite can be attributed to the presence of chitosan, a constituent of the composites, which indiscriminately adsorbs both gases.[51,52] Of note, under a flow of Xe and Kr diluted in air, pure HKUST-1 demonstrates a cumulated adsorption capacity of 3.18 mmol.g^{-1} for Xe and 1.92 mmol.g^{-1} for Kr.[53] The influence of chitosan under these conditions would be of interest to evaluate.

3. CONCLUSION

HKUST-1@CS composite beads with different compositions were successfully prepared using different drying methods and then assessed for gas (CO_2, CH_4, Xe, Kr) capture by adsorption at different operating conditions. The results presented herein together show increased gas sorption capacity when dried by treatment with supercritical CO_2 or by freeze-drying rather than by thermal evacuation methods, giving well-preserved macrostructures and enhanced porosity.

The adsorbents exhibit high surface areas (up to 502 $m^2 g^{-1}$) with excellent adsorption performance (CO_2 adsorption capacity in the range of 0.99 - 1.98 mmol g^{-1} at 298 K at 1 bar) and relatively low heats of adsorption (below 22.6 kJ mol^{-1}). Importantly, **HKUST-1@CS$_{1:1}$C** beads showed high equilibrium selectivities for CO_2/CH_4 separation (up to 6.8), suggesting that they are potential adsorbents for CO_2 separation. Finally, **HKUST-1@CS$_{1:1}$C** also exhibited interesting performances for Xe separation from Kr with a predicted Xe/Kr selectivity up to 6.2 at 273 K and 1.0 bar, which should be further looked upon.

Supporting Information

General bibliography; additional characterization of samples by SEM, XRD, XPS, EDS, FTIR, TGA, mercury intrusion porosimetry and N_2-physisorption isotherms; tables with additional experimental data; additional CO_2 adsorption isotherms and thermodynamic calculations.

Acknowledgment

The Chevreul Institute is thanked for its help in the development of this work through the ARCHI-CM project supported by the “Ministere de l’Enseignement Superieur de la Recherche et de l’Innovation”, the region “Hauts-de-France”, the ERDF program of the European Union and the “Metropole Europeenne de Lille. The region “Hauts-de-France” is also thanked for its support through the REGCAT project and UPCAT projects. The authors would like to thank Martine

Trentesaux for her help in carrying out the work on the Raman Spectroscopy Analysis, Laurence Burylo for the powder X-Ray diffraction and diffusion facility, Anne-Marie Blanchenet for SEM analyses, Pardis Simon for XPS analyses and Ridvan Yildiz from CERAMATHS laboratory for mercury intrusion.

References

(1) Li, H.; Li, L.; Lin, R.-B.; Zhou, W.; Zhang, Z.; Xiang, S.; Chen, B. Porous Metal-Organic Frameworks for Gas Storage and Separation: Status and Challenges. *EnergyChem* **2019**, 1, 100006.

(2) Cavenati, S.; Grande, C. A.; Rodrigues, A. E. Adsorption Equilibrium of Methane, Carbon Dioxide, and Nitrogen on Zeolite 13X at High Pressures. *J. Chem. Eng. Data* **2004**, 49, 1095–1101.

(3) Balou, S.; Babak, S. E.; Priye, A. Synergistic Effect of Nitrogen Doping and Ultra-Microporosity on the Performance of Biomass and Microalgae-Derived Activated Carbons for CO2 Capture. *ACS Appl. Mater. Interfaces* **2020**, 12, 42711–42722.

(4) Jiang, C.; Wang, X.; Ouyang, Y.; Lu, K.; Jiang, W.; Xu, H.; Wei, X.; Wang, Z.; Dai, F.; Sun, D. Recent Advances in Metal–Organic Frameworks for Gas Adsorption/Separation. *Nanoscale Adv.* **2022**, 4, 2077–2089.

(5) Zhou. H-C; Long. J.R.; Yaghi. O. M. Introduction to Metal–Organic Frameworks. *Chem. Rev.* **2012**, 112, 673–674.

(6) Abdelhamid, H. N. Removal of Carbon Dioxide Using Zeolitic Imidazolate Frameworks: Adsorption and Conversion via Catalysis. *Appl. Organomet. Chem.* **2022**, 36, e6753.

(7) Bazer-Bachi, D.; Assié, L.; Lecocq, V.; Harbuzaru, B.; Falk, V. Towards Industrial Use of Metal-Organic Framework: Impact of Shaping on the MOF Properties. *Powder Technol.* **2014**, 255, 52–59.

(8) Yeskendir, B.; Dacquin, J.-P.; Lorgouilloux, Y.; Courtois, C.; Royer, S.; Dhainaut, J. From Metal–Organic Framework Powders to Shaped Solids: Recent Developments and Challenges. *Mater. Adv.* **2021**, 2 (22), 7139–7186.

(9) Abramova, A.; Couzon, N.; Leloire, M.; Nerisson, P.; Cantrel, L.; Royer, S.; Loiseau, T.; Volkringer, C.; Dhainaut, J. Extrusion-Spheronization of UiO-66 and UiO-66_NH2 into Robust-Shaped Solids and Their Use for Gaseous Molecular Iodine, Xenon, and Krypton Adsorption. *ACS Appl. Mater. Interfaces* **2022**, 14, 10669–10680.

(10) Kitagawa, S. Future Porous Materials. Acc. Chem. Res. **2017**, 50, 514–516.

(11) El Hankari, S.; Bousmina, M.; El Kadib, A. Biopolymer@Metal-Organic Framework Hybrid Materials: A Critical Survey. *Prog. Mater. Sci*. **2019**, 106, 100579.

(12) Hammi, N.; El Hankari, S.; Katir, N.; Marcotte, N.; Draoui, K.; Royer, S.; El Kadib, A. Polysaccharide Templated Biomimetic Growth of Hierarchically Porous Metal-Organic Frameworks. *Micropor. Mesopor. Mat.* **2020**, 306, 110429.

(13) Hammi, N.; Chen, S.; Primo, A.; Royer, S.; Garcia, H.; El Kadib, A. Shaping MOF Oxime Oxidation Catalysts as Three-Dimensional Porous Aerogels through Structure-Directing Growth inside Chitosan Microspheres. *Green Chem*. **2022**, 24, 4533–4543.

(14) Ding, M.; Cai, X.; Jiang, H.-L. Improving MOF Stability: Approaches and Applications. *Chem. Sci.* **2019**, 10, 10209–10230.

(15) Fan, X.; Zhang, L.; Zhang, G.; Shu, Z.; Shi, J. Chitosan Derived Nitrogen-Doped Microporous Carbons for High Performance CO2 Capture. *Carbon* **2013**, 61, 423–430.

(16) Chagas, J. A. O.; Crispim, G. O.; Pinto, B. P.; San Gil, R. A. S.; Mota, C. J. A. Synthesis, Characterization, and CO2 Uptake of Adsorbents Prepared by Hydrothermal Carbonization of Chitosan. *ACS Omega* **2020**, 5, 29520–29529.

(17) Oliveira, D. E. F.; Chagas, J. A. O.; de Lima, A. L.; Mota, C. J. A. CO2 Capture over MCM-41 and SBA-15 Mesoporous Silicas Impregnated with Chitosan. *Ind. Eng. Chem. Res*. **2022**, 61, 10522–10530.

(18) Alhwaige, A. A.; Ishida, H.; Qutubuddin, S. Carbon Aerogels with Excellent CO2 Adsorption Capacity Synthesized from Clay-Reinforced Biobased Chitosan-Polybenzoxazine Nanocomposites. *ACS Sustainable Chem. Eng*. **2016**, 4, 1286–1295.

(19) Fan, M.; Gai, F.; Cao, Y.; Zhao, Z.; Ao, Y.; Liu, Y.; Huo, Q. Structuring ZIF-8-Based Hybrid Material with Hierarchical Pores by in Situ Synthesis and Thermal Treatment for Enhancement of CO2 Uptake. *J. Solid State Chem*. **2019**, 269, 507–512.

(20) Bueken, B.; Van Velthoven, N.; Willhammar, T.; Stassin, T.; Stassen, I.; Keen, D. A.; Baron, G. V.; Denayer, J. F. M.; Ameloot, R.; Bals, S.; De Vos, D.; Bennett, T. D. Gel-Based Morphological Design of Zirconium Metal–Organic Frameworks. *Chem. Sci*. **2017**, 8, 3939–3948.

(21) Park, H. J.; Lim, D.-W.; Yang, W. S.; Oh, T.-R.; Suh, M. P. A Highly Porous Metal–Organic Framework: Structural Transformations of a Guest-Free MOF Depending on Activation Method and Temperature. *Chem. Eur. J*. **2011**, 17, 7251–7260.

(22) Ma, L.; Jin, A.; Xie, Z.; Lin, W. Freeze Drying Significantly Increases Permanent Porosity and Hydrogen Uptake in 4,4-Connected Metal–Organic Frameworks. *Angew. Chem. Int. Ed*. **2009**, 48, 9905–9908.

(23) Valentin, R.; Molvinger, K.; Quignard, F.; Brunel, D. Supercritical CO2 Dried Chitosan: An Efficient Intrinsic Heterogeneous Catalyst in Fine Chemistry. *New J. Chem*. **2003**, 27, 1690–1692.

(24) Huo, J.; Brightwell, M.; El Hankari, S.; Garai, A.; Bradshaw, D. A Versatile, Industrially Relevant, Aqueous Room Temperature Synthesis of HKUST-1 with High Space-Time Yield. *J. Mater. Chem. A* **2013**, 1, 15220–15223.

(25) El Kadib, A.; Primo, A.; Molvinger, K.; Bousmina, M.; Brunel, D. Nanosized Vanadium, Tungsten and Molybdenum Oxide Clusters Grown in Porous Chitosan Microspheres as Promising Hybrid Materials for Selective Alcohol Oxidation. *Chem. Eur. J*. **2011**, 17, 7940–7946.

(26) Jagódka, P.; Matus, K.; Łamacz, A. On the HKUST-1/GO and HKUST-1/RGO Composites: The Impact of Synthesis Method on Physicochemical Properties. *Molecules* **2022**, 27, 7082.

(27) Denning, S.; Majid, A. A.; Lucero, J. M.; Crawford, J. M.; Carreon, M. A.; Koh, C. A. Metal–Organic Framework HKUST-1 Promotes Methane Hydrate Formation for Improved Gas Storage Capacity. *ACS Appl. Mater. Interfaces* **2020**, 12, 53510–53518.

(28) Dhainaut, J.; Piana, G.; Deville, S.; Guizard, C.; Klotz, M. Freezing-Induced Ordering of Block Copolymer Micelles. *Chem. Commun*. **2014**, 50, 12572–12574.

(29) Chartier, C.; Buwalda, S.; Van Den Berghe, H.; Nottelet, B.; Budtova, T. Tuning the Properties of Porous Chitosan: Aerogels and Cryogels. International Journal of Biological *Macromolecules* **2022**, 202, 215–223.

(30) Nelson, A. P.; Farha, O. K.; Mulfort, K. L.; Hupp, J. T. Supercritical Processing as a Route to High Internal Surface Areas and Permanent Microporosity in Metal−Organic Framework Materials. *J. Am. Chem. Soc.* **2009**, 131, 458–460.

(31) Huang, G.; Chen, J.; Tang, X.; Xiong, D.; Liu, Z.; Wu, J.; Sun, W.-Y.; Lin, B. Facile Method To Prepare a Novel Biological HKUST-1@CMCS with Macroscopic Shape Control for the Long-Acting and Sustained Release. *ACS Appl. Mater. Interfaces* **2019**, 11, 10389–10398.

(32) Basumallick, S.; Rajasekaran, P.; Tetard, L.; Santra, S. Hydrothermally Derived Water-Dispersible Mixed Valence Copper-Chitosan Nanocomposite as Exceptionally Potent Antimicrobial Agent. *J Nanopart Res*. **2014**, 16, 2675.

(33) Jennah, O.; Beniazza, R.; Lozach, C.; Jardel, D.; Molton, F.; Duboc, C.; Buffeteau, T.; El Kadib, A.; Lastécouères, D.; Lahcini, M.; Vincent, J.-M. Photoredox Catalysis at Copper(II) on Chitosan: Application to Photolatent CuAAC. *Adv. Synth. Catal*. **2018**, 360, 4615–4624.

(34) Vrtovec, N.; Mazaj, M.; Buscarino, G.; Terracina, A.; Agnello, S.; Arčon, I.; Kovač, J.; Zabukovec Logar, N. Structural and CO2 Capture Properties of Ethylenediamine-Modified HKUST-1 Metal–Organic Framework. *Cryst. Growth Des.* **2020**, 20, 5455–5465.

(35) Xu, F.; Yu, Y.; Yan, J.; Xia, Q.; Wang, H.; Li, J.; Li, Z. Ultrafast Room Temperature Synthesis of GrO@HKUST-1 Composites with High CO2 Adsorption Capacity and CO2/N2 Adsorption Selectivity. *Chem. Eng. J.* **2016**, 303, 231–237.

(36) Yang, C.; Zhao, T.; Pan, H.; Liu, F.; Cao, J.; Lin, Q. Facile Preparation of N-Doped Porous Carbon from Chitosan and NaNH2 for CO2 Adsorption and Conversion. *J. Chem. Eng*. **2022**, 432, 134347.

(37) Singh, G.; Lee, J.; Karakoti, A.; Bahadur, R.; Yi, J.; Zhao, D.; AlBahily, K.; Vinu, A. Emerging Trends in Porous Materials for CO2 Capture and Conversion. *Chem. Soc. Rev*. **2020**, 49, 4360–4404.

(38) Hsan, N.; Dutta, P. K.; Kumar, S.; Bera, R.; Das, N. Chitosan Grafted Graphene Oxide Aerogel: Synthesis, Characterization and Carbon Dioxide Capture Study. *Int. J. Biol. Macromol*. **2019**, 125, 300–306.

(39) Hammi, N.; Couzon, N.; Loiseau, T.; Volkringer, C.; El Kadib, A.; Royer, S.; Dhainaut, J. Hierarchically Porous ZIF-67/Chitosan Beads with High Surface Area and Strengthened Mechanical Properties: Application to CO2 Storage. *Mater. Today Sustain*. **2023**, 22, 100394.

(40) Alhwaige, A. A.; Agag, T.; Ishida, H.; Qutubuddin, S. Biobased Chitosan Hybrid Aerogels with Superior Adsorption: Role of Graphene Oxide in CO2 Capture. *RSC Adv*. **2013**, 3, 16011–16020.

(41) Barrulas, R. V.; López-Iglesias, C.; Zanatta, M.; Casimiro, T.; Mármol, G.; Carrott, M. R.; García-González, C. A.; Corvo, M. C. The AEROPILs Generation: Novel Poly(Ionic Liquid)-Based Aerogels for CO2 Capture. *Int. J. Mol. Sci*. **2022**, 23, 200.

(42) Kumar, S.; de A. e Silva, J.; Wani, M. Y.; Dias, C. M. F.; Sobral, A. J. F. N. Studies of Carbon Dioxide Capture on Porous Chitosan Derivative. *J Dispers Sci Technol*. **2016**, 37, 155–158.

(43) Jiang, M.; Li, H.; Zhou, L.; Xing, R.; Zhang, J. Hierarchically Porous Graphene/ZIF-8 Hybrid Aerogel: Preparation, CO2 Uptake Capacity, and Mechanical Property. *ACS Appl. Mater. Interfaces* **2018**, 10, 827–834.

(44) Xia, Y.; Mokaya, R.; Walker, G. S.; Zhu, Y. Superior CO2 Adsorption Capacity on N-Doped, High-Surface-Area, Microporous Carbons Templated from Zeolite. *Adv. Energy Mater.* **2011**, 1, 678–683.

(45) Primo, A.; Forneli, A.; Corma, A.; García, H. From Biomass Wastes to Highly Efficient CO2 Adsorbents: Graphitisation of Chitosan and Alginate Biopolymers. *ChemSusChem* **2012**, 5, 2207–2214.

(46) Liu, Y.; Ye, Q.; Shen, M.; Shi, J.; Chen, J.; Pan, H.; Shi, Y. Carbon Dioxide Capture by Functionalized Solid Amine Sorbents with Simulated Flue Gas Conditions. *Environ. Sci. Technol.* **2011**, 45, 5710–5716.

(47) Dhainaut, J.; Bonneau, M.; Ueoka, R.; Kanamori, K.; Furukawa, S. Formulation of Metal–Organic Framework Inks for the 3D Printing of Robust Microporous Solids toward High-Pressure Gas Storage and Separation. *ACS Appl. Mater. Interfaces* **2020**, 12, 10983–10992.

(48) Spanopoulos, I.; Tsangarakis, C.; Klontzas, E.; Tylianakis, E.; Froudakis, G.; Adil, K.; Belmabkhout, Y.; Eddaoudi, M.; Trikalitis, P. N. Reticular Synthesis of HKUST-like Tbo-MOFs with Enhanced CH4 Storage. *J. Am. Chem. Soc*. **2016**, 138, 1568–1574.

(49) Tripodi, A.; Conte, F.; Rossetti, I. Carbon Dioxide Methanation: Design of a Fully Integrated Plant. *Energy Fuels* **2020**, 34, 7242–7256

(50) Abid, H. R.; Hanif, A.; Keshavarz, A.; Shang, J.; Iglauer, S. CO2, CH4, and H2 Adsorption Performance of the Metal–Organic Framework HKUST-1 by Modified Synthesis Strategies. *Energy Fuels* **2023**, 37, 7260–7267.

(51) Sikora, B. J.; Wilmer, C. E.; Greenfield, M. L.; Snurr, R. Q. Thermodynamic Analysis of Xe/Kr Selectivity in over 137 000 Hypothetical Metal–Organic Frameworks. *Chem. Sci*. **2012**, 3, 2217–2223.

(52) Banerjee, D.; Simon, C. M.; Plonka, A. M.; Motkuri, R. K.; Liu, J.; Chen, X.; Smit, B.; Parise, J. B.; Haranczyk, M.; Thallapally, P. K. Metal–Organic Framework with Optimally Selective Xenon Adsorption and Separation. *Nat. Commun.* **2016**, 7, ncomms11831.

(53) Liu, J.; Thallapally, P. K.; Strachan, D. Metal–Organic Frameworks for Removal of Xe and Kr from Nuclear Fuel Reprocessing Plants. *Langmuir* **2012**, 28, 11584–11589.

Table of Contents